

Phase-separated porous nanocomposite with ultralow percolation threshold for wireless bioelectronics

In the format provided by the
authors and unedited

The PDF file includes:

Supplementary Notes 1 to 4

Supplementary Figures 1 to 31

Supplementary Tables 1 to 2

Captions for the Supplementary Videos

Supplementary References

Other Supplementary Information for this manuscript includes the following:

Supplementary Videos 1 to 4

Supplementary Note 1. Theoretical calculation of electrical resistance under strain

The underlying microscopic mechanisms that govern the electromechanical performance of porous and nonporous Ag NWs nanocomposites could be explored through numerical calculations. For these computations, we assume that the Ag NWs have a consistent diameter ($D = 40$ nm) and length ($L = 30$ μ m). Note that both the porous (porosity, 60%) and nonporous nanocomposites contain an equivalent number of Ag NWs within a specified volume of the PU matrix ($2 \times 10^7 / \text{mm}^2$). We adopted a network resistor model¹ to characterize the connectivity and resistance of the NWs in the nanocomposite, and the resistance of the total network was calculated using Kirchhoff's current law and Ohm's law. We categorized the junctions formed between two NWs based on their relative distances. These categories are as follows:

(i) Complete contact: If the shortest distance (d) between the centerlines of two adjacent NWs is less than or equal to the diameter (D) of a NW, the NWs are deemed to be in full contact. In this study, we assume that the contact resistance between two adjacent Ag NWs is negligible.

(ii) Tunneling junction: This category involves a scenario where two NWs aren't in direct contact, but they are close enough for electron tunneling to occur. Specifically, tunneling can happen when the distance (d) exceeds D but remains below a specified cutoff distance (d_{cutoff}). Here, we choose $d_{cutoff} = 50 \cdot D$. And the tunneling resistance was given by²:

$$R_{tunnel} = \frac{h^2 d}{A e^2 \sqrt{2m\lambda}} e^{\left(\frac{4\pi d}{h} \sqrt{2m\lambda}\right)}$$

where e is the elementary charge, m is the mass of electron, h is the Planck's constant, d is the distance between the centerlines of two adjacent Ag NWs, λ is the energy barrier (1 eV), and A is the cross-sectional area of the tunnel and is approximated to be the cross-sectional area of an individual Ag NW.

(iii) Complete disconnection: This denotes scenarios where two NWs are spaced far enough apart ($d > d_{cutoff}$) that neither direct contact nor electron tunneling can take place.

To examine the variations in resistance under strain, the reposition and reorientation of Ag NWs caused by tensile stretch is evaluated using the 3D fiber reorientation model³. Ag NWs were assigned to random positions (x, y, z) with random orientations (in plane angle θ , out of plane angle φ) within the PU matrix. Under a local strain along x-axis (ε), the center coordinates of Ag NW (x, y, z) are changed to:

$$\begin{aligned} x' &= x(1 + \varepsilon) \\ y' &= y(1 + \varepsilon)^{-\nu} \\ z' &= z(1 + \varepsilon)^{-\nu} \end{aligned}$$

where x' , y' and z' are the new center coordinates of the Ag NW under strain and ν is the Poisson's ration of the nanocomposite (0.4). And the orientation of the Ag NW (θ, φ) tends to shift towards:

$$\begin{aligned} \theta^* &= \tan^{-1}[(1 + \varepsilon)^{-\nu-1} \tan \theta] \\ \varphi^* &= \cos^{-1}[(1 + \varepsilon)^{-\nu} \cos \varphi] \end{aligned}$$

And the final orientation of Ag NW is given by:

$$\theta' = \tan^{-1}[(1 - \alpha) \tan \theta + \alpha \tan \theta^*]$$

$$\varphi' = \cos^{-1}[(1 - \alpha) \cos \varphi + \alpha \cos \varphi^*]$$

where α is a constant denoting the ease with which the fiber changes its orientation under strain. When $\alpha = 1$, the fiber alters its orientation freely in tandem with the matrix deformation. Conversely, $\alpha = 0$ indicates that the fiber maintains its original orientation irrespective of matrix deformation. Here, we choose $\alpha = 0.1$ for simulation.

Porous nanocomposite. Given the phase-separated nature of the porous nanocomposite, where the Ag NWs self-assemble on the pore surface, we posit that all the Ag NWs exclusively align on the inner curvilinear surfaces of the PU microstructures. Similarly, Ag NWs were assigned to random positions (x, y) with random orientations (θ) on the pore surface. We employed the commercial software ABAQUS to study mechanics of the porous nanocomposite and analyze the local strains exerted on the PU microstructure under global strains. Once we have the local strains, we applied the algorithm described above to calculate resistance change of the nanocomposite under strain.

Mechanism. When the 3D microstructure is macroscopically stretched, the bridging elements within the spongy-like structures first deform and rotate to the direction of stretching to accommodate the global strain. Local strains exerted on the PU microstructure, at this stage, mainly involves bending strains, and therefore are small compared with the global strains. On the other hand, while the bridging elements rotate under strain, Ag NWs would have more contacts with each other, thus diminishing the resistance degradation. Taken together, these possibilities fall into the benefits of multiscale porous polymer matrices that dissipate stress and rigid conductive fillers that adapt to strain-induced geometry changes during stretching.

Supplementary Note 2. Theoretical calculation of percolation thresholds

Nonporous nanocomposite. Based on the assumption that the nanofillers are homogeneously dispersed in the polymer matrix with each conductive filler occupying one single unit, the percolation threshold of nonporous composites ($V_{NP,c}$) only depends on the form factors of the conductive fillers and can be theoretically expressed as follows when one-dimensional (1D) nanowires are used as filler materials⁴.

$$V_{NP,c} = \frac{27\pi d^2}{4l^2}$$

where d and l are the diameter and length of the 1D nanowires.

Porous nanocomposite with self-organized Ag NWs on pore surface. Given the morphology of our porous Ag NWs nanocomposite, Ag NWs are selectively distributed on pore surface to create percolation networks (Fig. 2a, left). Therefore, we assume that all Ag NWs are uniformly distributed on a continuously interconnected curved surface (area, S) within the three-dimensional porous polymer matrices. This gives rise to the minimum number of nanowires required to achieve percolation pathways N_c .

$$N_c = S \cdot n_c$$

where n_c is the critical density (i.e., number of fillers per unit area), and S is the area of the curved surface, which is determined by the pore size (D_p) of the microstructures, i.e., $S = f(D_p)$. The critical density with random 1D filler distribution is given by Monte Carlo simulations⁵.

$$n_c l^2 = 5.63726$$

The critical volume of Ag NWs (V_{AgNWs}) in the porous nanocomposite can be calculated by:

$$V_{AgNWs} = \frac{1}{4} \pi d^2 l N_c$$

The percolation threshold ($V_{P,c}$) of the porous nanocomposite is defined as:

$$V_{P,c} = \frac{V_{AgNWs}}{V}$$

where V is the total volume of the porous nanocomposite.

Finally, the percolation threshold for the porous nanocomposite is obtained.

$$V_{P,c} = \frac{1.4093\pi d^2}{Vl} f(D_p)$$

For simplicity, a porous structure with uniform spherical pores is used to represent the interconnected porous structures. Here, center-to-center distance is set to be $0.45D_p$. Calculation is performed in COMOSL-Multiphysics and the results are plotted in Fig. 1f.

Supplementary Note 3. Effect of pore size on electrical conductivity

Given the assumption stated in Supplementary Note 2, the number of Ag NWs per unit area (filler density, N) is given by:

$$N = \frac{N_{total}}{S} = \frac{N_{total}}{f(D_p)}$$

The electrical conductivity (σ) is positively correlated with conductive filler density according to the standard percolation theory⁶:

$$\sigma \propto (N - N_c)^\alpha$$

Therefore, we could get:

$$\sigma \propto \left(\frac{N_{total}}{f(D_p)} - \frac{5.63726f(D_p)}{l^2} \right)^\alpha$$

where N_{total} is number of Ag NWs in the porous nanocomposite, l is the length of the nanowires, N_c is the critical nanowire density, D_p is the pore size, and α is a critical exponent (typically $\sim 1.3-2$)⁷, respectively.

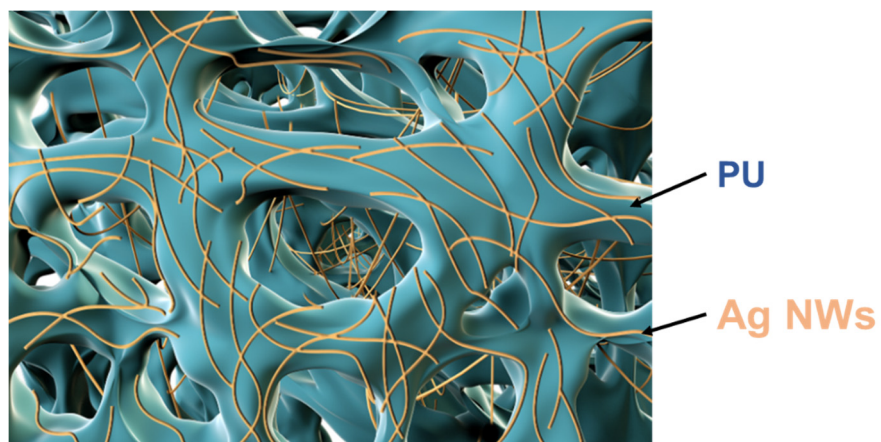
For a given filler content (constant N_{total}), large pore size (D_p) gives rise to small surface area (S), and thus large number of Ag NWs per unit area (N). Finally, we could conclude that large pore size and higher filler density benefit for the higher electrical conductivity.

Supplementary Note 4. Experimental extraction of percolation threshold using 3D percolation theory

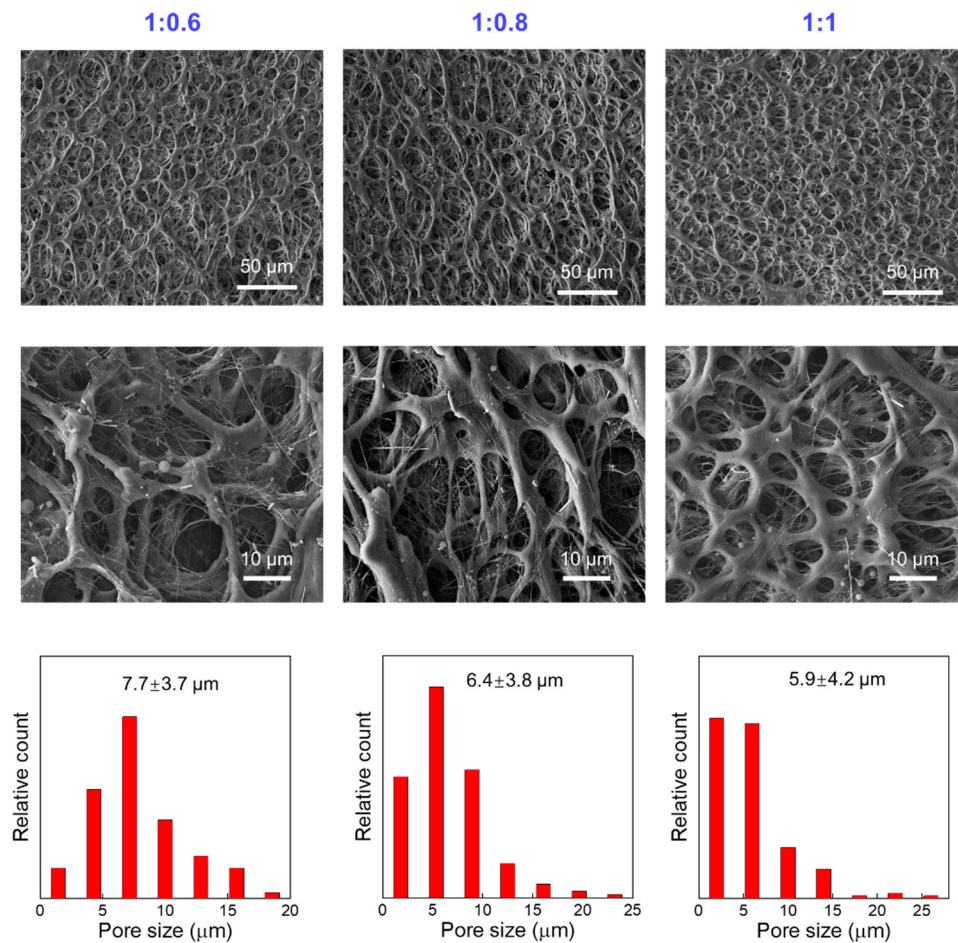
Experimental data of electrical conductivities as a function of Ag NWs volume fractions in the nanocomposite (Fig. 2b) were fitted using 3D percolation theory, which is given by⁸:

$$\sigma = \sigma_0(V_f - V_c)^s$$

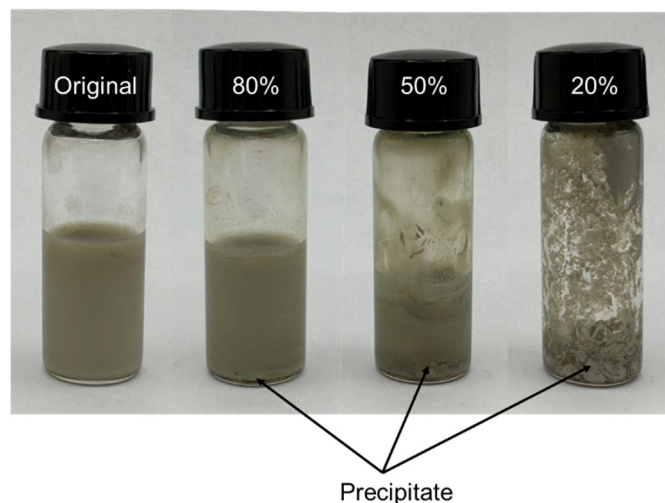
Where σ and σ_0 denote the electrical conductivity of the nanocomposite and the bulk Ag. V_f , V_c , and s are the volume fraction of Ag NWs, percolation threshold, and exponent factor, respectively. Here the bulk Ag conductivity (σ_0) is $8.5 \times 10^5 \text{ S cm}^{-1}$. The values of V_c and s are obtained by fitting the experimental data for nanocomposites with different Ag NWs volume fractions.



Supplementary Figure 1. Schematic of porous microstructures of PSPN in three dimensions. The microscale pores are interconnected throughout the PU matrices.

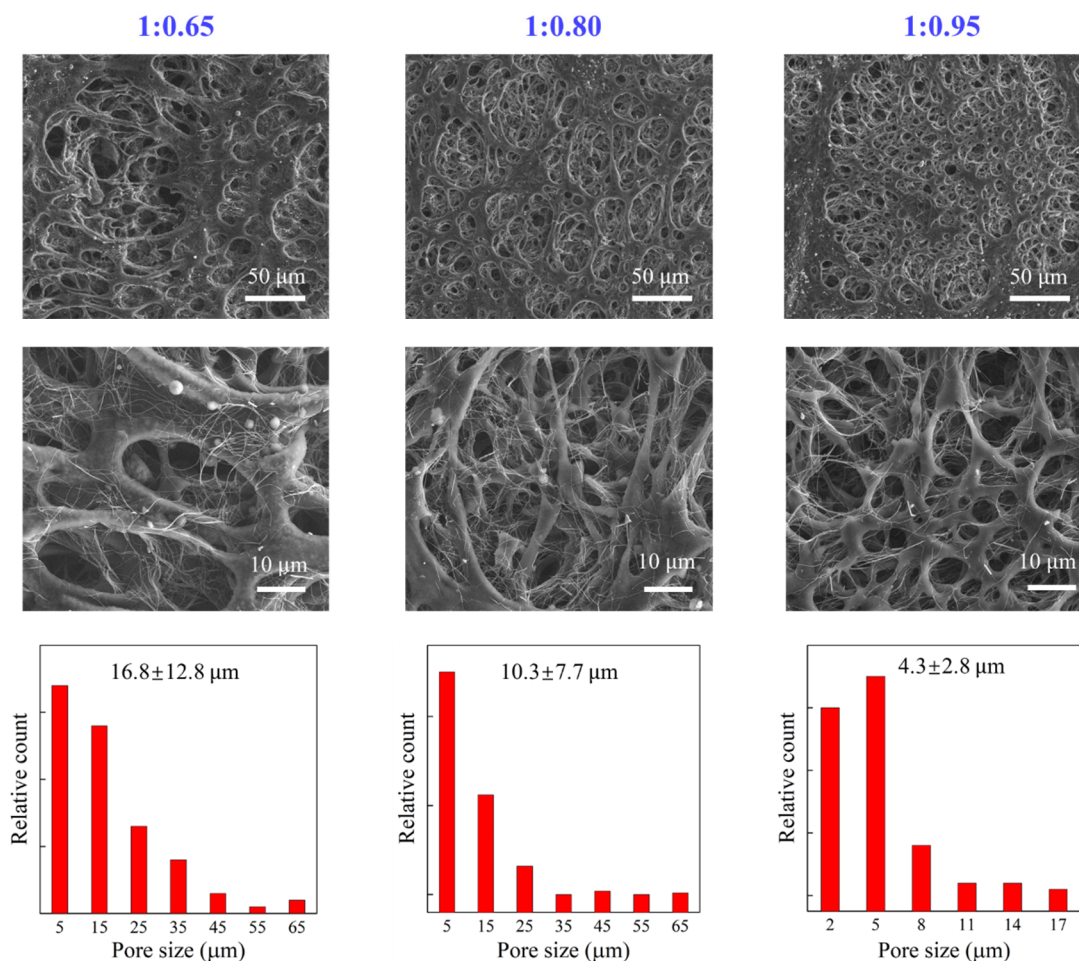


Supplementary Figure 2. SEM images and corresponding particle size distributions of PSPN. Here, 1 ml of PU solution (70 mg/ml in THF) and 0.4 ml of Ag NWs solution (20 mg/ml in ethanol) were first mixed, followed by the addition of ethanol (0.2, 0.4, and 0.6 ml) to vary the nonsolvent content. Quantitative analysis indicates that the pore size slightly decreases with the increase of ethanol volume content.

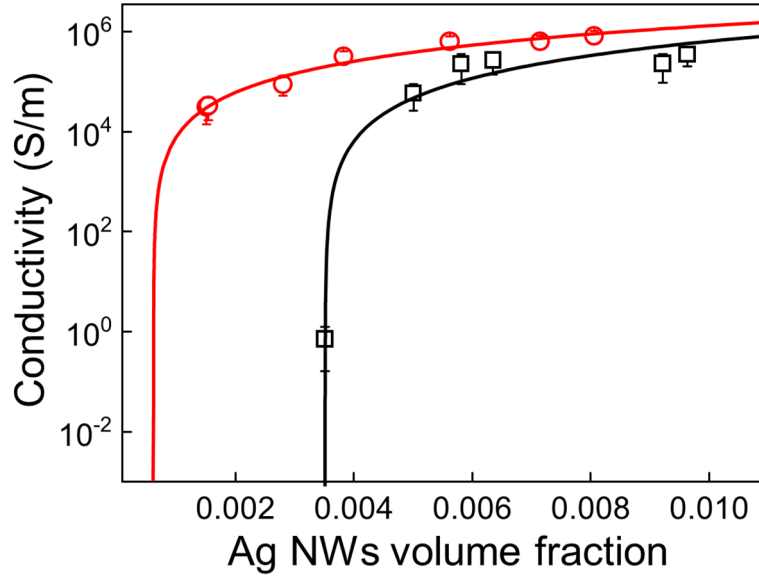


Supplementary Figure 3. Photographs of nanocomposite solutions with different initial compositions.

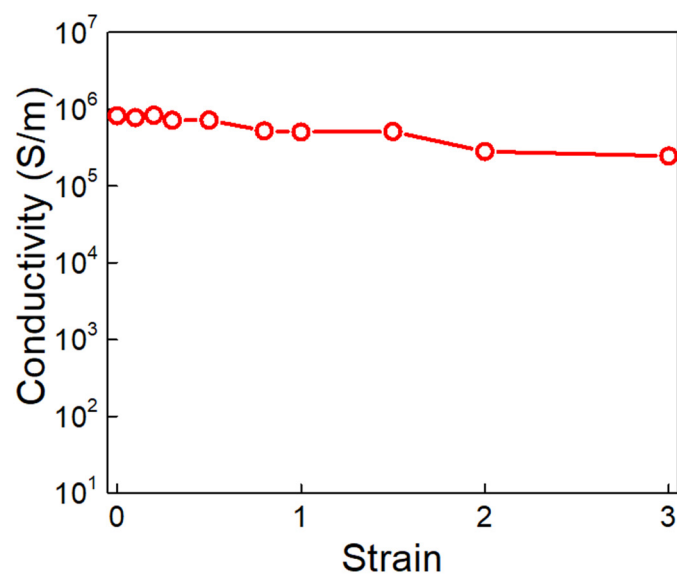
We intentionally decreased the amounts of THF and ethanol in the precursor solutions while keeping the amounts of PU and silver nanowires constant. Specifically, we prepared precursor solutions with 80%, 50%, and 20% of the original THF and ethanol amounts. After 24 hours of continuous sonication in a bath sonicator, visible PU precipitates were still present in the solutions, as shown in the optical image below, which prevented us from making a uniform porous nanocomposite film by using phase separation. Indeed, this observation highlights the importance of our method, which takes advantage of natural thermal evaporation under ambient conditions.



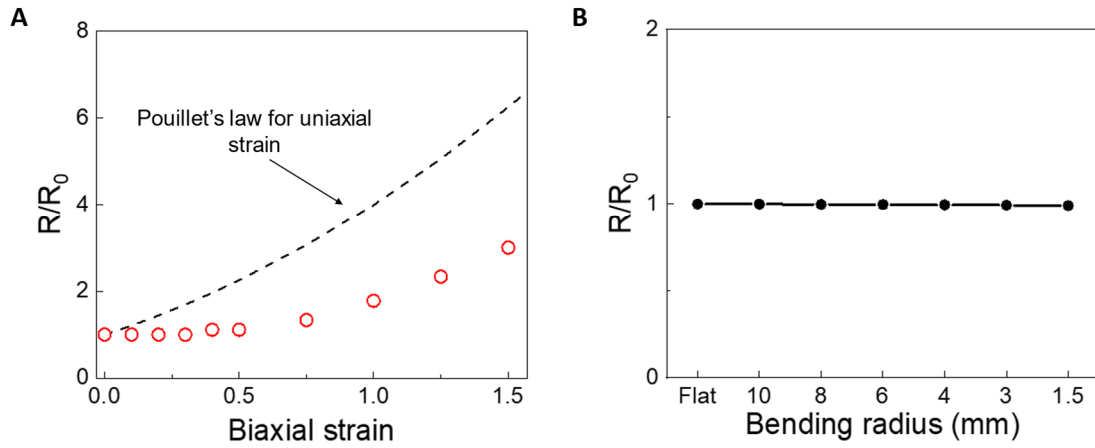
Supplementary Figure 4. SEM images and corresponding particle size distributions of PSPN with 1-butanol. Here, we introduced 1-butanol as co-nonsolvent to tune the pore size. Specifically, 1 ml of PU solution (70 mg/ml in THF) and 0.4 ml of Ag NWs solution (20 mg/ml in ethanol) were first mixed, followed by the additions of 1-butanol (0.25, 0.4, and 0.55 ml). Quantitative analysis indicates that the pore size decreases while porosity increases (49.3%, 63.2%, 64.8%) with the increase of co-nonsolvent volume content.



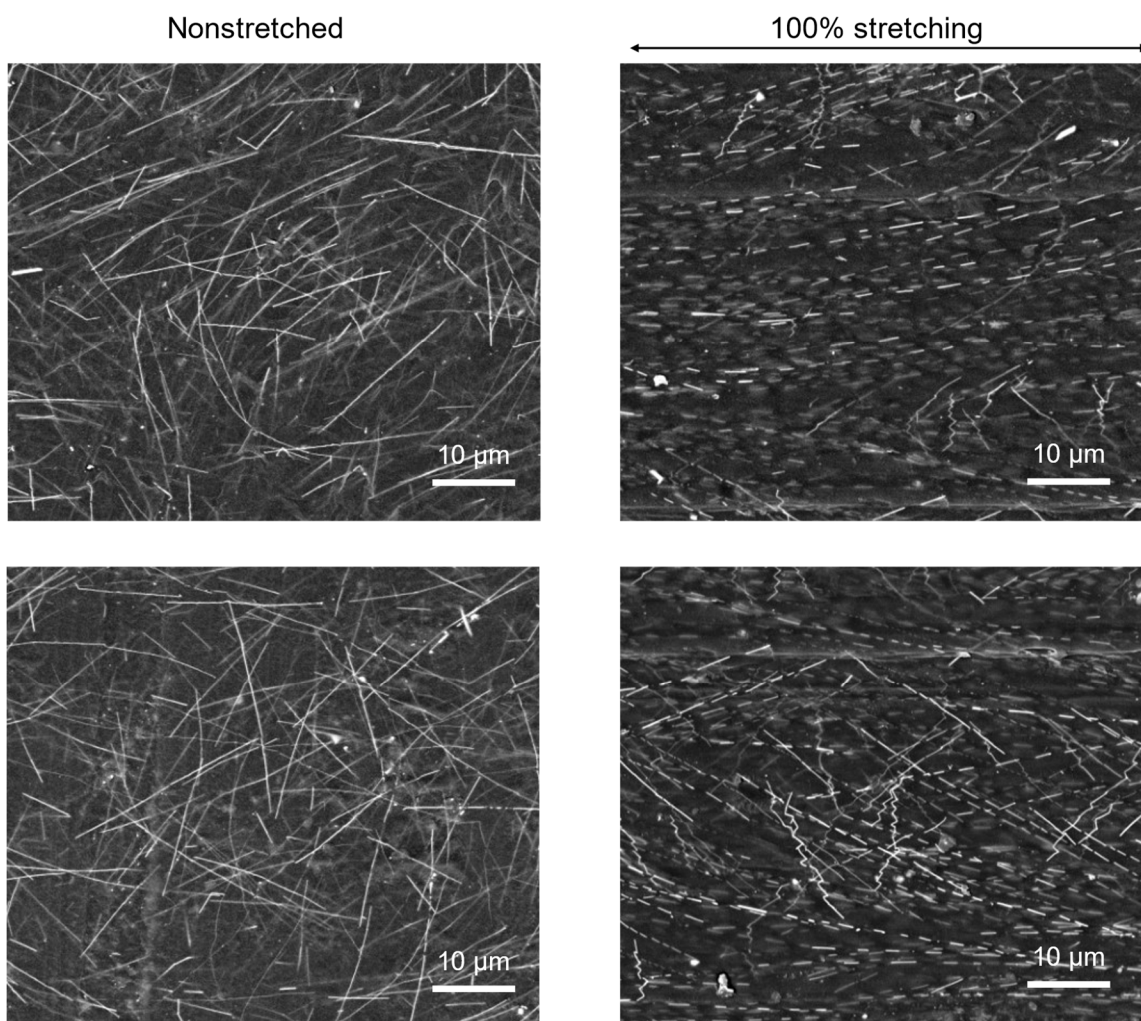
Supplementary Figure 5. Percolation thresholds of PSPN with 1-butanol. Electrical conductivities of PSPN with 1-butanol with tunable pore sizes (red circle, ~16.8 μm ; black square, ~4.3 μm) as a function of Ag NWs volume fractions. Data are fitted using the 3D percolation theory. This experimental observation aligns with our theoretical analysis presented in Fig. 1f, indicating that the percolation threshold is influenced by pore size. Specifically, there were a 48-fold ($V_c=0.00062$) and 8.5-fold ($V_c=0.00351$) decrease in the threshold compared with nonporous nanocomposite (Fig. 2b) when the pore size was changed to ~16.8 and ~4.3 μm . Error bars represent standard deviations of the mean from six samples.



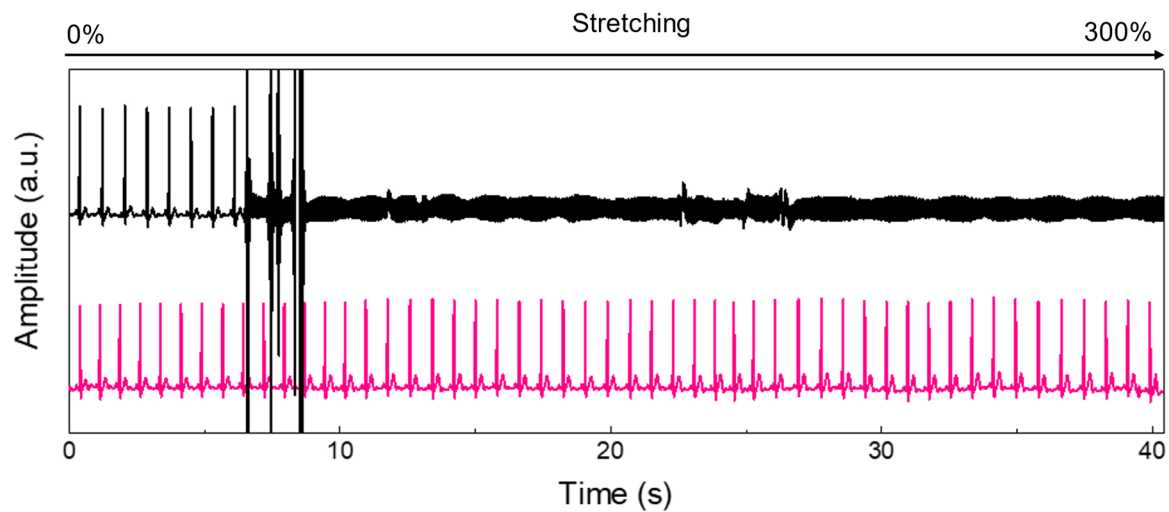
Supplementary Figure 6. Conductivity–strain characteristics of the phase-separated porous Ag NWs nanocomposite. The electrical conductivity was examined by a previously reported four-probe method⁹.



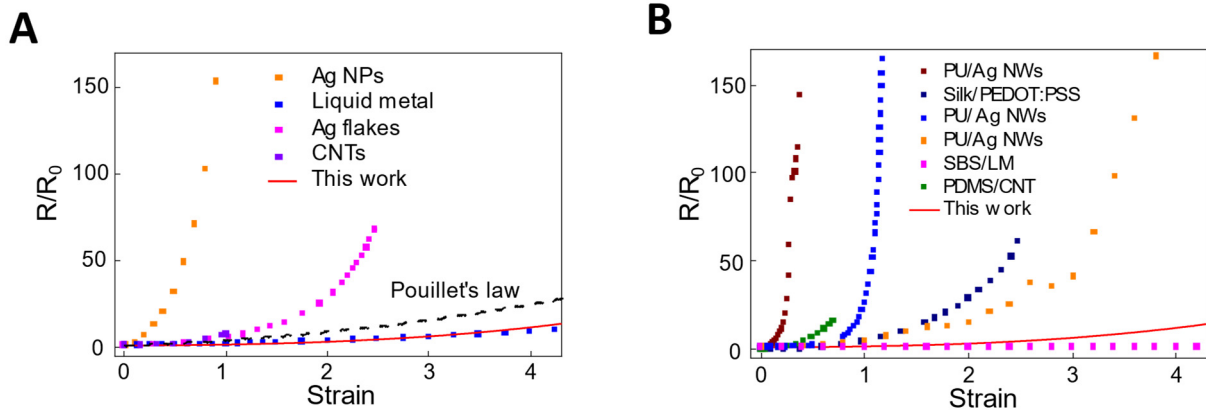
Supplementary Figure 7. Electromechanical performance of PSPN under biaxial stretching (A) and bending (B). Pouillet's law [$R/R_0 = (1 + \varepsilon)^2$] that assumes a classical incompressible, constant-conductivity bulk conductor under strain was plotted as a comparison.



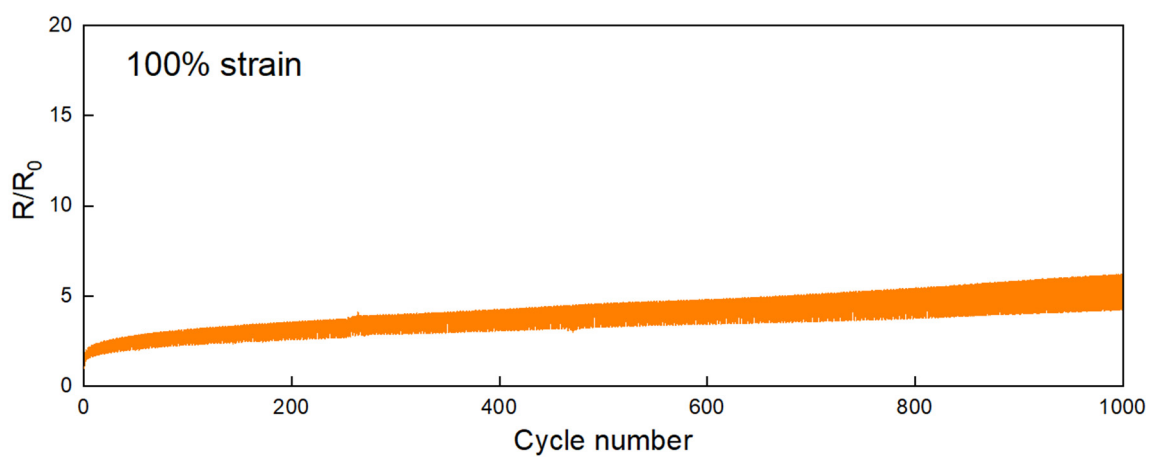
Supplementary 8. SEM images of nonporous Ag NWs nanocomposite before (left) and after (right) 100% strain. The stretched sample exhibits evident breakage of Ag NWs percolation networks and therefore leads to substantially reduced electrical conductivity. This observation aligns with recent report on nonporous Ag NWs nanocomposites¹⁰.



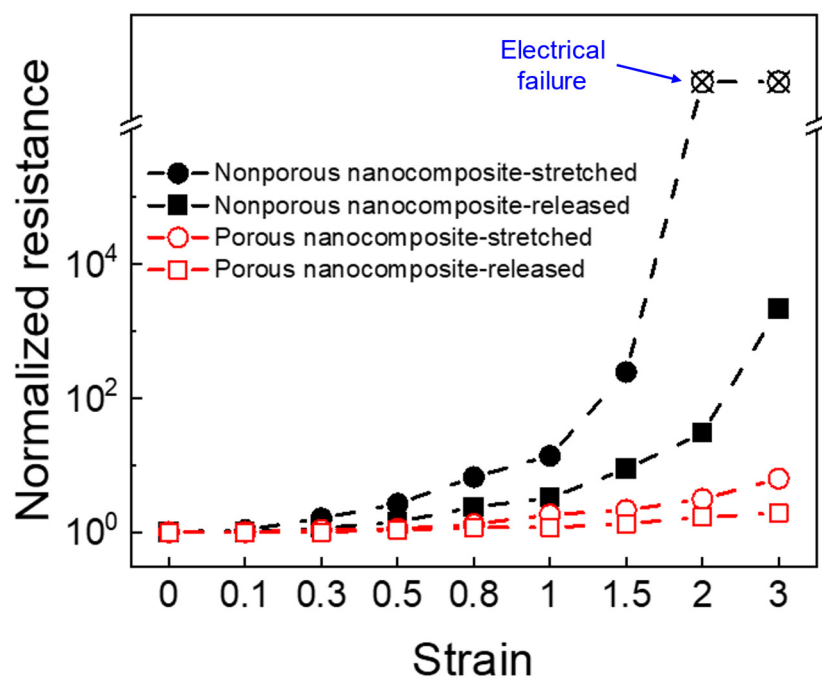
Supplementary Figure 9. Real-time electrocardiogram signals recorded with electrical wiring made of our PSPN (red) and conventional Ag NWs (black) when stretched from 0% to 300% strain. Our porous nanocomposite allows for high-fidelity signal recording with negligible signal degradation for more than 300% strain, while the conventional Ag NWs fails to operate at small strain.



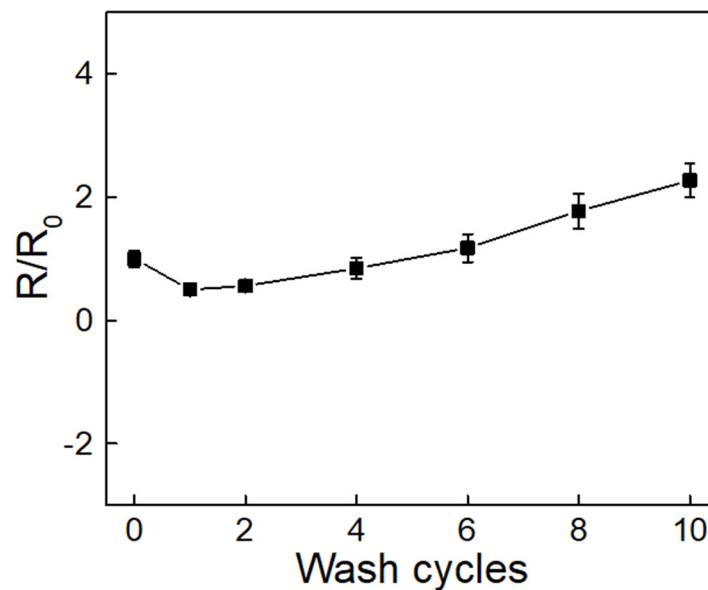
Supplementary Figure 10. Comparison of electromechanical characteristics with Pouillet's law and other reported nonporous (A) and porous (B) elastic conductors. Nonporous conductors (A) include Ag nanoparticles (Ag NPs)¹¹, liquid metal¹², Ag flakes¹³, and carbon nanotubes¹⁴-based composites; and porous conductors (B) include PU/Ag NWs (dark red)¹⁵, Silk/PEDOT:PSS¹⁶, PU/Ag NWs (blue)¹⁷, PU/Ag NWs (orange)¹⁸, SBS/LM¹⁹, and PDMS/CNT²⁰ composites.



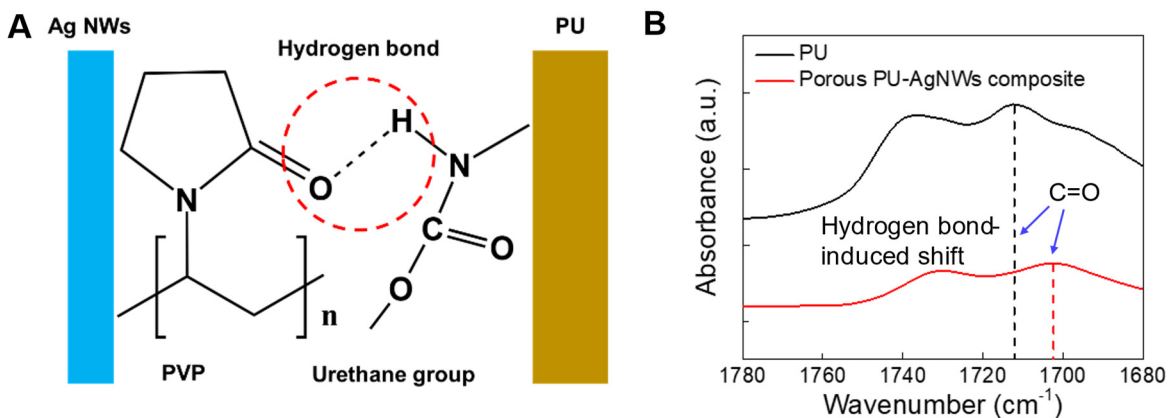
Supplementary Figure 11. Relative resistance changes of the phase-separated porous Ag NWs nanocomposites subjected to cyclic stretching (100% maximum strain) for 1,000 cycles.



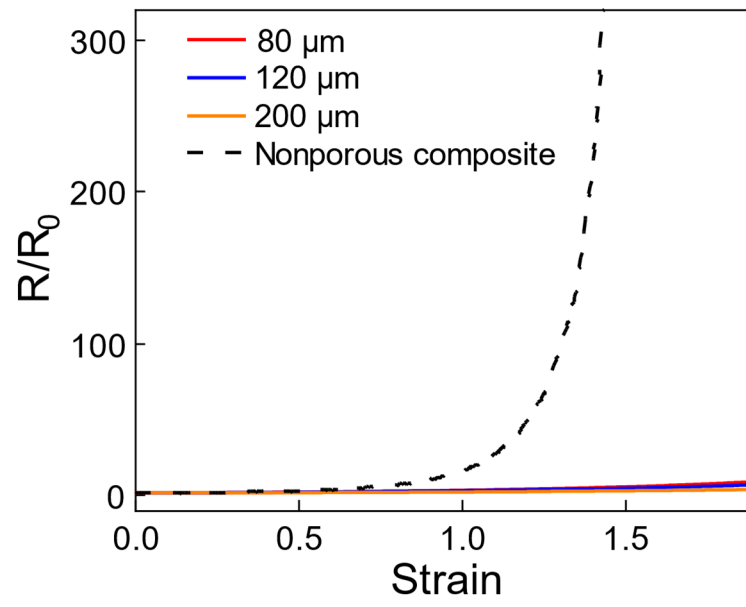
Supplementary Figure 12. Normalized resistance changes of the phase-separated porous (red) and nonporous (black) Ag NWs nanocomposites at stretched and released states after ethanol treatment. Results show that ethanol can effectively assist the recovery of resistance for porous nanocomposites, whereas there is negligible effect on nonporous nanocomposites.



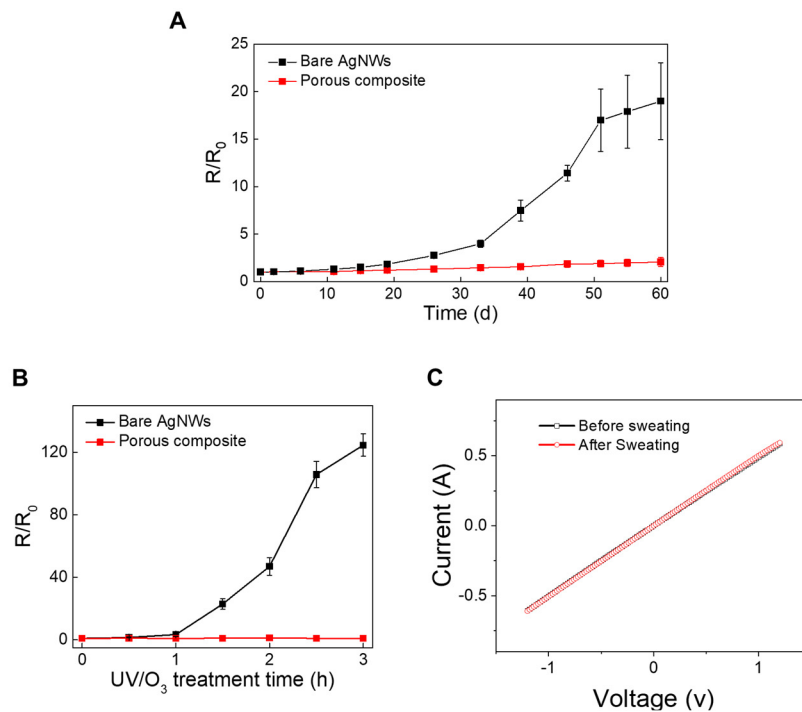
Supplementary Figure 13. Normalized resistance variations of PSPN after repetitive washing cycles (20 min for each cycle) in soap, showing the robustness and durability. The decrease of resistance in the first cycle is attributed to the soap added in the solution, which resulted in autocatalytic addition of dissolved silver ions to the nanowire junction²¹. Error bars represent standard deviations of the mean from three samples.



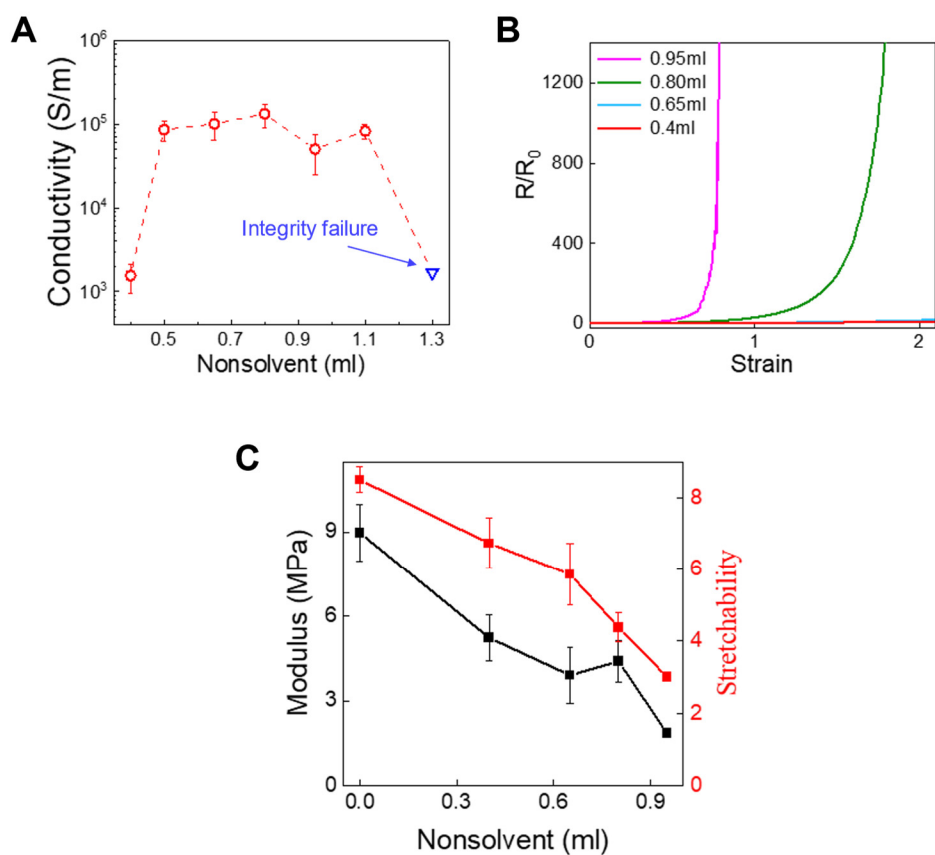
Supplementary Figure 14. Tough interface between Ag NWs and porous PU matrix. (A) Schematic of hydrogen bonding between the amphiphilic ligand (PVP) and PU. **(B)** A comparison of Fourier-transform infrared spectroscopy (FTIR) spectra on PU matrix (black), and PSPN (red). The peak of the carbonyl group shifted to smaller wavenumbers, indicating the formation of hydrogen bonding¹⁸.



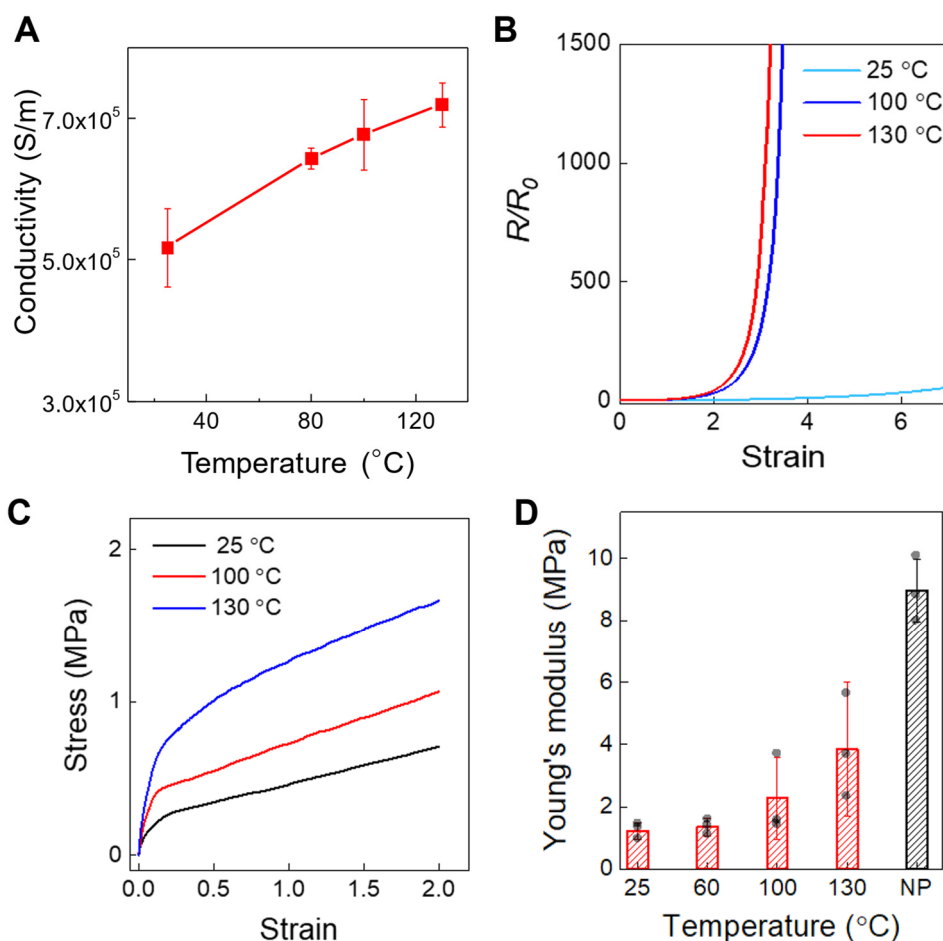
Supplementary Figure 15. Electromechanical performance analysis of PSPN with various thicknesses. Results demonstrate that varying the thickness of PSPN has a trivial impact on its electromechanical performance.



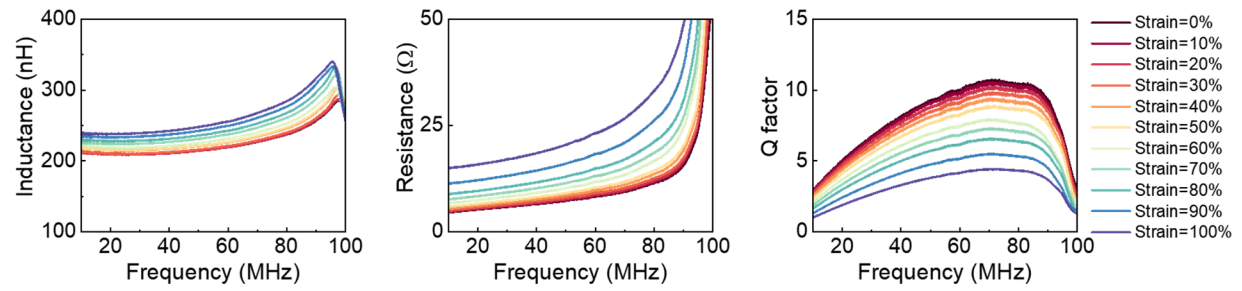
Supplementary Figure 16. Stability tests of PSPN. Resistance changes of bare Ag NWs and porous Ag NWs nanocomposite (PSPN) under ambient condition (A) and UV Ozone treatment (B). (C) I-V curves of PSPN before and after 30 mins of wearing with heavy skin perspiration. Error bars represent standard deviations of the mean from three samples.



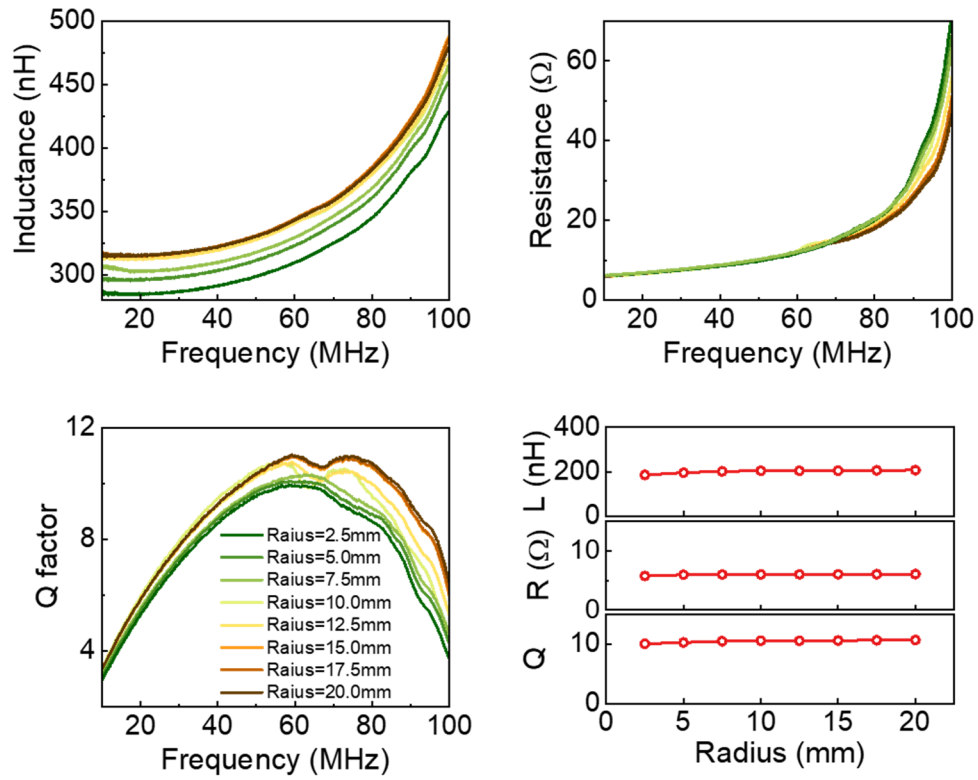
Supplementary Figure 17. Investigation of the effect of nonsolvent on electrical conductivity (A), electromechanical property (B), and modulus and maximum stretchability (C) of the resulting PSPN with 1-butanol. Error bars represent standard deviations of the mean from three samples. In this experiment, 1 ml of PU solution (70 mg/ml in THF) was combined with an equivalent volume of silver nanowire (Ag NWs) solution (0.4 ml, 20 mg/ml in ethanol) to ensure a consistent amount of Ag NWs was employed. Subsequently, varying amounts of 1-butanol were introduced to modulate the nonsolvent content.



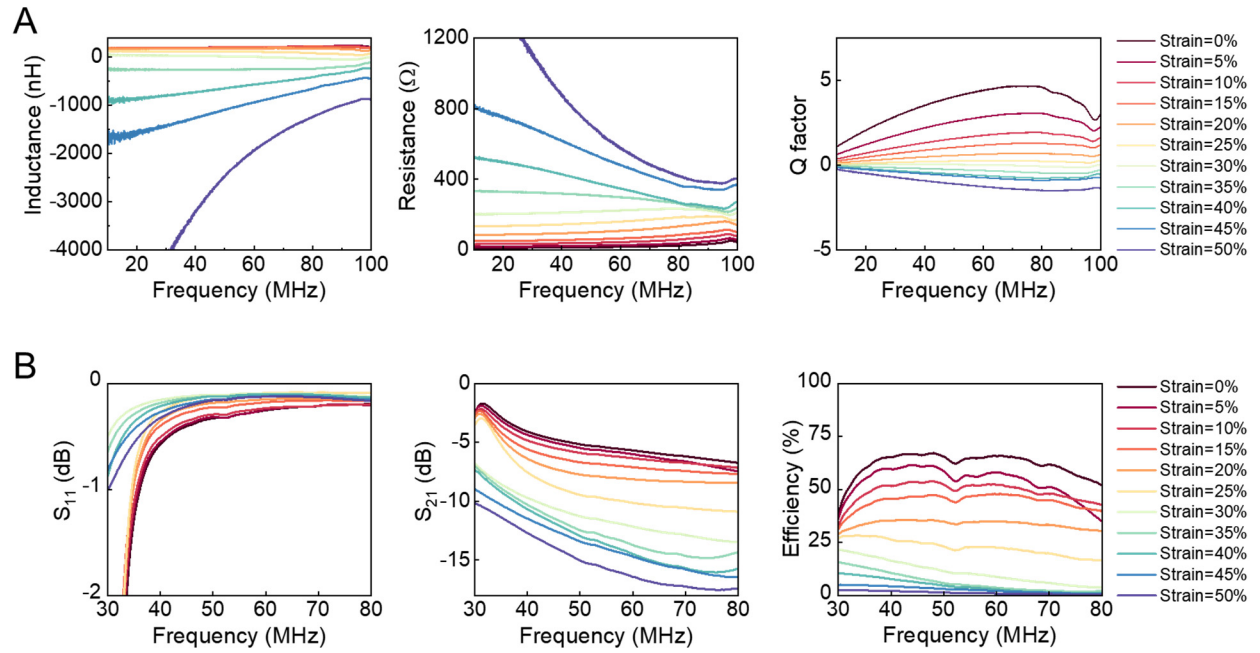
Supplementary Figure 18. Investigation of the effect of post-annealing temperature on electrical conductivity (A), electromechanical property (B), stress-strain curves (C), and Young's modulus (D) of the resulting PSPN with 1-butanol. Error bars represent standard deviations of the mean from three samples. Here, the PSPN with 1-butanol were prepared by mixing 1 ml of PU solution (70 mg/ml in THF) with 0.4 ml of Ag NWs solution (20 mg/ml in ethanol) and 0.4 ml of 1-butanol. Thermal annealing was carried out for 20 min at various temperatures. NP represents nonporous Ag NWs nanocomposites.



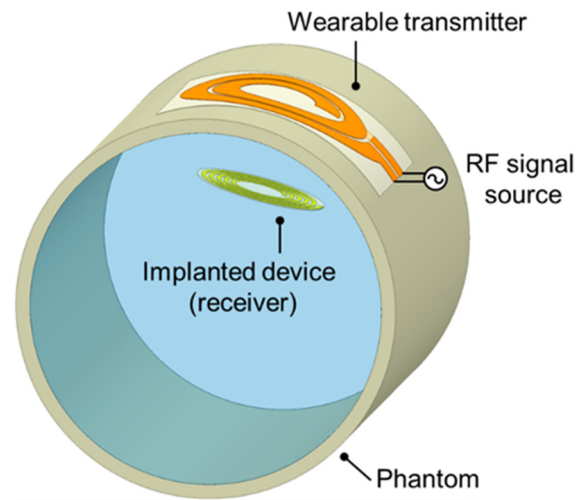
Supplementary Figure 19. Evolutions of inductance (left), resistance (middle), and Q factor (right) of the PSPN coil as functions of frequency under various strains.



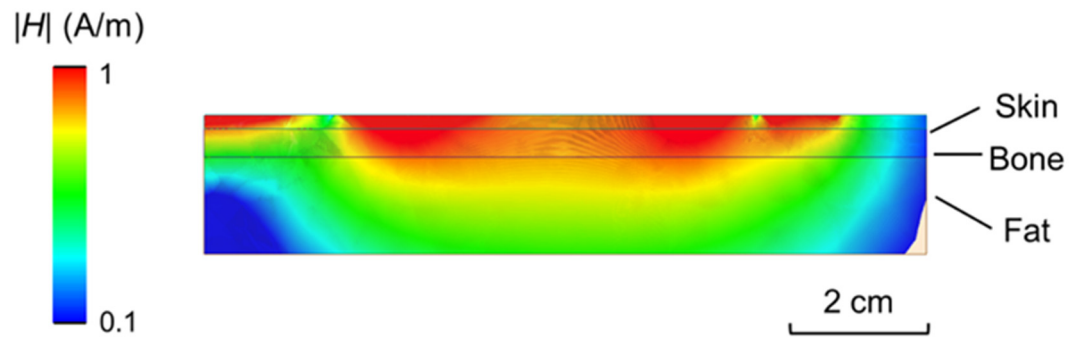
Supplementary Figure 20. Variations of inductance, resistance, and Q factor of the PSPN coil under various bending radii.



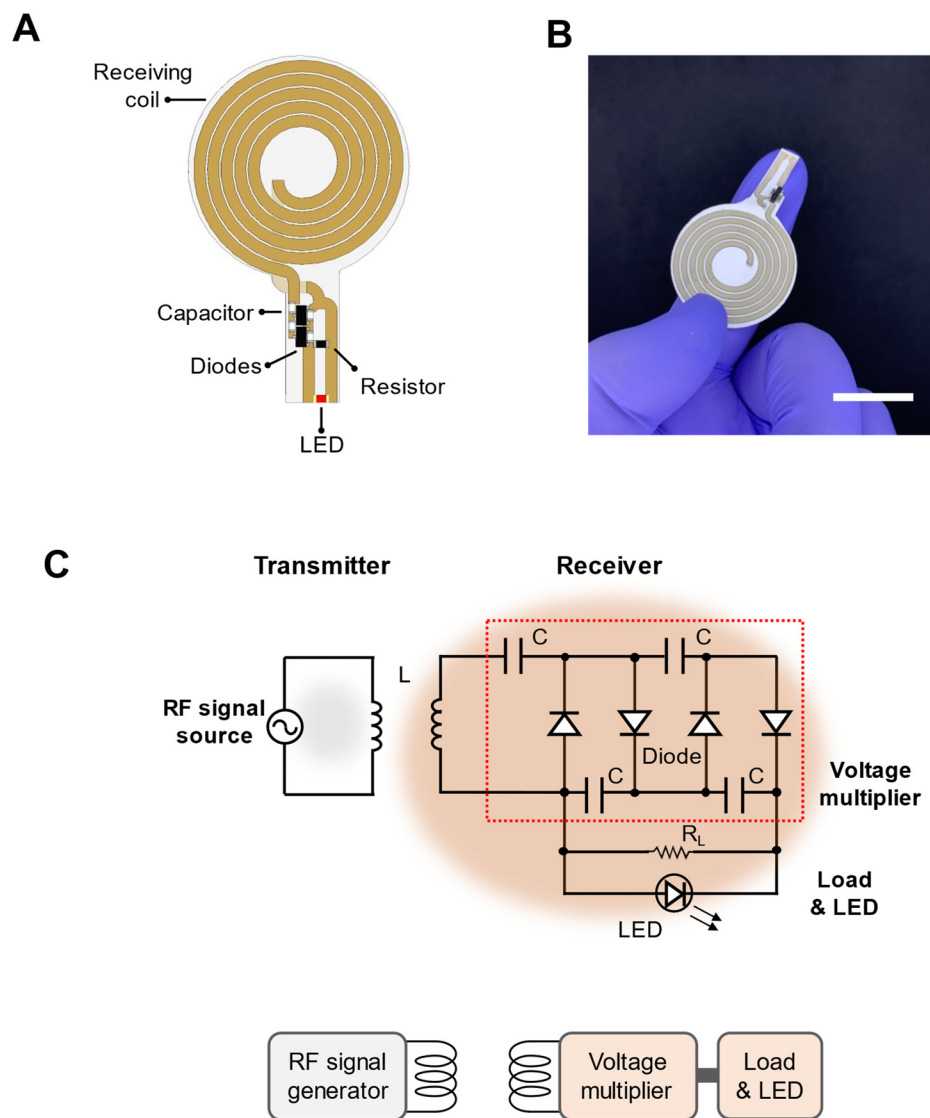
Supplementary Figure 21. Characteristics of the conventional nonporous Ag NWs coil. (A) Evolutions of inductance (left), resistance (middle), and Q factor (right) of the nonporous Ag NWs coil as functions of frequency under various strains. **(B)** Scattering parameters S_{11} (left), S_{21} (middle), and efficiency (right) of the WPT system with conventional nonporous Ag NWs coil under various strains.



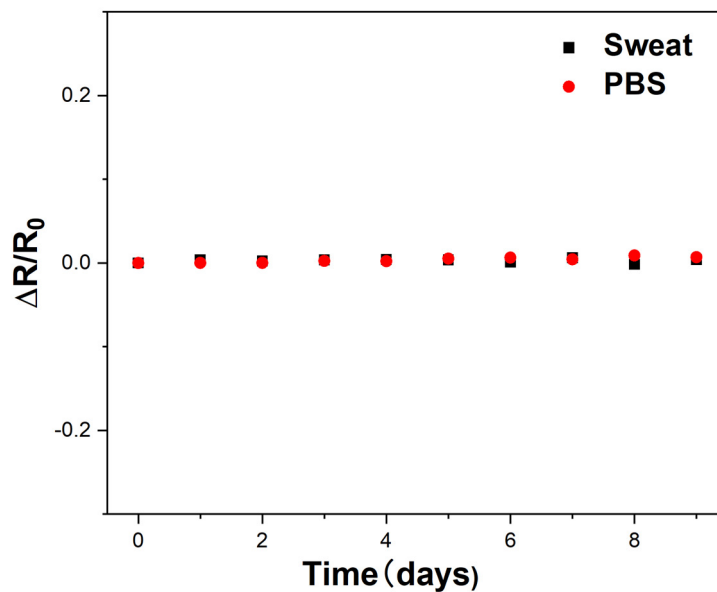
Supplementary Figure 22. Schematic of the phantom setup used for measurements of coupling coefficient and transfer efficiency under strain.



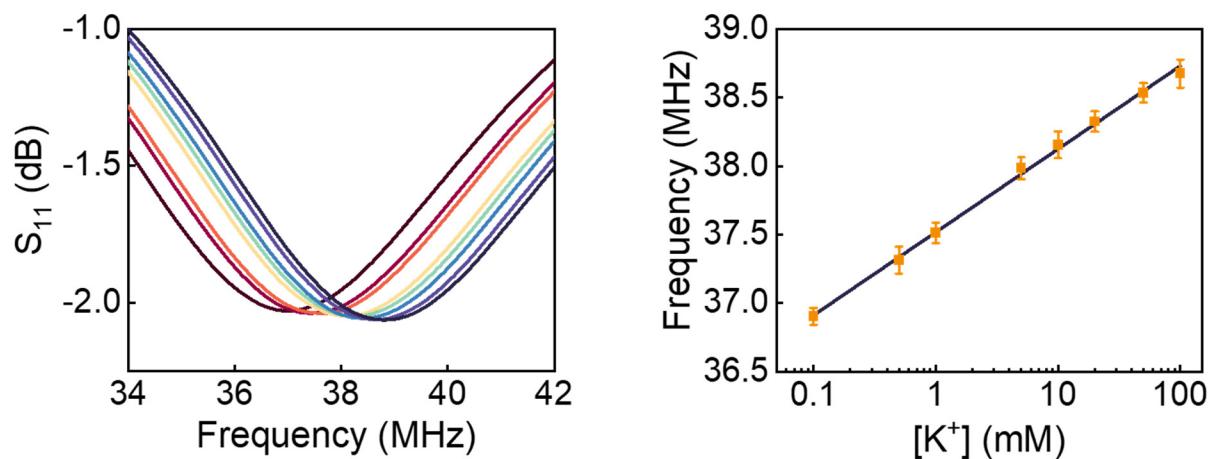
Supplementary Figure 23. Maxwell simulation of the magnetic field generated by a soft transmitter placed on flat human skin. Using Ansys Maxwell for simulation, we observed that the magnetic field can effectively penetrate human skin, bone, and fat, showcasing potential for powering biomedical implants.



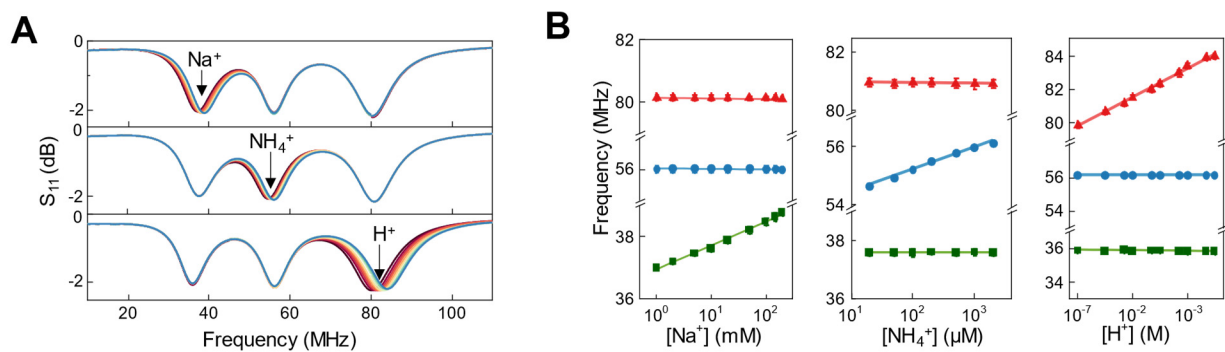
Supplementary Figure 24. Implantable optoelectronic device. Schematic (A), photograph (B), and working mechanism (C) of the implantable optoelectronic device. The RF power is wirelessly transferred to the receiver coil through inductive coupling, rectified and multiplied by the voltage multiplier, and delivered to the load and LED. The diode used is SMS7621-005LF from Skyworks. The capacitor and resistor values are 1000 pF and 1 M Ω , respectively. Scale bar, 2cm.



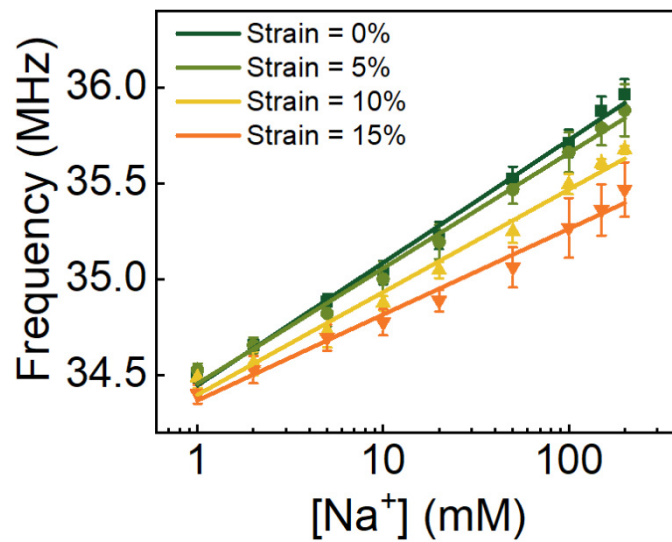
Supplementary Figure 25. Stability tests of the optoelectronic device encapsulated with silicone in PBS and artificial sweat. There were negligible degradations when stored in PBS (pH 7.4) and artificial perspiration (pH 4.3, Pickering Laboratories) for nine days at room temperature.



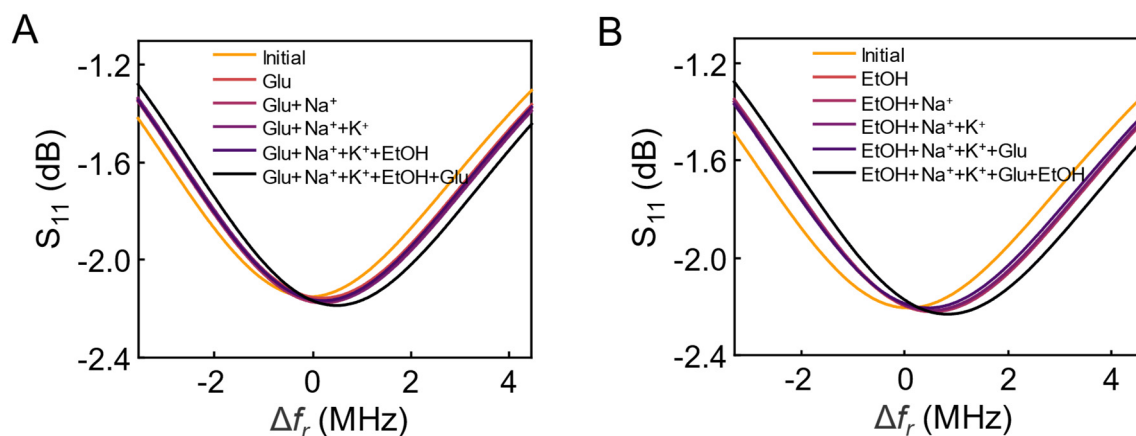
Supplementary Figure 26. Wireless monitoring of biomarkers using PSPN-based NFC antenna. Measured reflection spectrum and frequency shifts of wireless K^+ sensor in response to various analyte concentrations in the wireless systems. Error bars represent standard deviations of the mean from three samples.



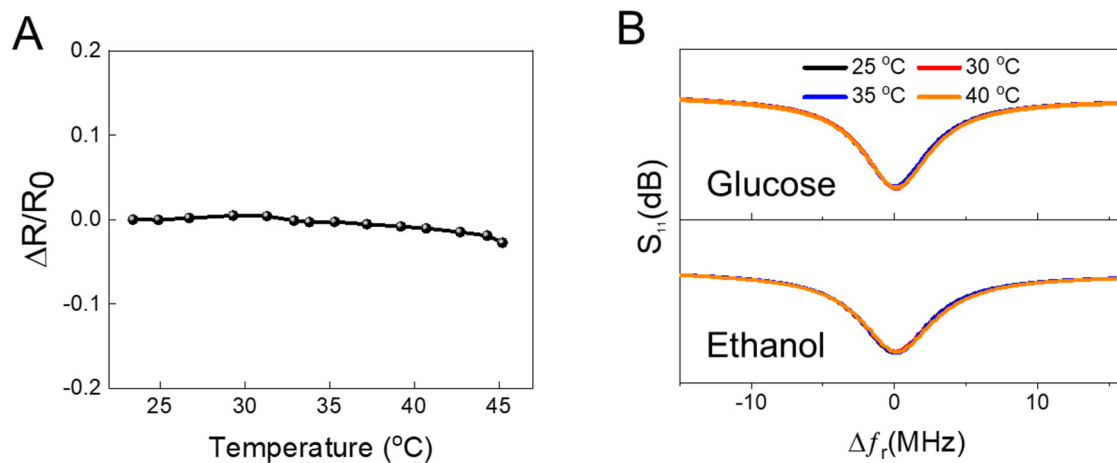
Supplementary Figure 27. Crosstalk of the multiplexed sensing system. (A) Reflection spectrum for the multiplexed sensing. **(B)** Cross-sensitivity extracted from (A), indicating negligible crosstalk among these sensors. Red, H^+ ; blue, NH_4^+ ; green, Na^+ .



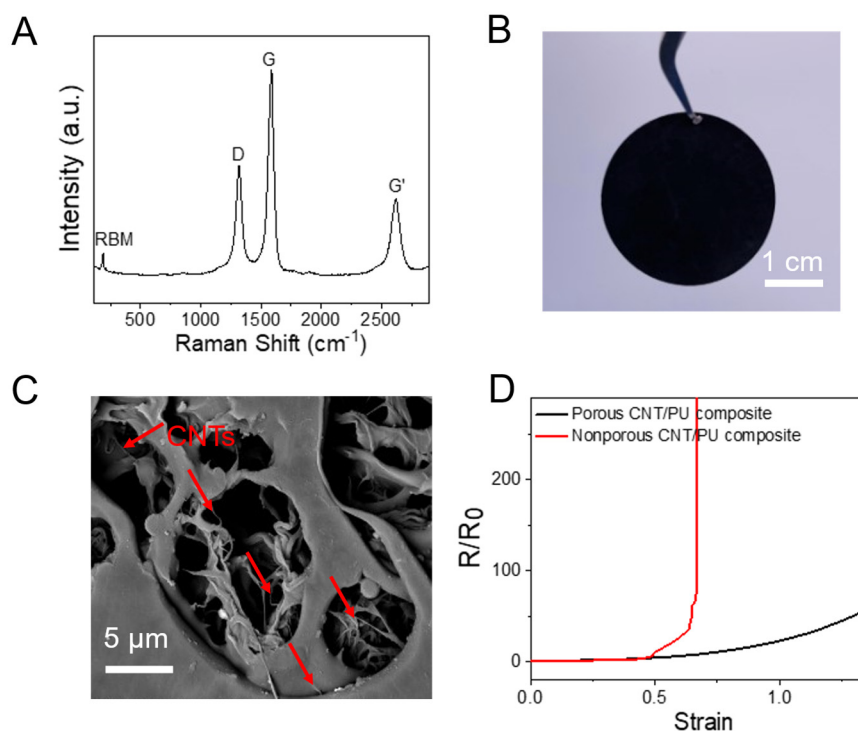
Supplementary Figure 28. Frequency shifts of the Na^+ sensor integrated with wireless data transmission antenna made of conventional Ag NWs coil under strain. Error bars represent standard deviations of the mean from three samples. Extracted sensitivity under strain present in Fig. 5f.



Supplementary Figure 29. Selectivity tests of the multiplexed sensing system. (A) Glucose sensor responses to the addition of target molecules and interfering biomarkers, including glucose (150 μ M), Na (20 mM), K (5 mM), ethanol (20 mM). **(B)** Alcohol sensor responses to the addition of target molecules and interfering biomarkers, including ethanol (20 mM), Na (20 mM), K (5 mM), glucose (150 μ M). Real-time changes of the frequency are extracted and shown in Fig. 5k.



Supplementary Figure 30. Effects of temperature variations on biochemical sensing of the PSPN-based wireless bioelectronic system. (A) Resistance variations of the PSPN coil under various temperatures (23 $^{\circ}\text{C}$ –45 $^{\circ}\text{C}$). **(B)** Responses of wireless alcohol and glucose sensors based on PSPN to coil temperature variations at 25 $^{\circ}\text{C}$, 30 $^{\circ}\text{C}$, 35 $^{\circ}\text{C}$, and 40 $^{\circ}\text{C}$, respectively.



Supplementary Figure 31. Phase-separated porous carbon nanotube (CNT) nanocomposite. (A) Raman spectrum of CNTs used as conductive fillers. Optical image (B) and SEM image (C) of the phase-separated porous CNT nanocomposites, showing self-organized CNT bundles within the porous PU microstructures. (D) Relative resistance change (R/R_0) of nonporous and phase-separated porous CNT nanocomposites as a function of uniaxial strains, indicating the superior electromechanical performance of the porous nanocomposite. Here, the porous CNT nanocomposite was prepared by mixing 5 ml of PU solution (70 mg/ml) with 4 ml of CNTs (900711, Sigma Aldrich) solution (2 mg/ml in ethanol with 1% sodium dodecylbenzene sulfonate), whereas the nonporous one was prepared by mixing identical PU solution with 15 mg of CNTs.

Supplementary Table 1 Comparisons of the PSPN with existing porous conductors.

Materials	Percolation threshold (V_c)	Stretchability	Conductivity (S/cm)	Breathability ($\text{g m}^{-2} \text{ day}^{-1}$)	R/R ₀ @100%	Ref.	
Porous metallic composites							
PDMS/AgNWs	0.0048 (wt.%)	1.4	42	Yes	1.4	22	
Ecoflex/AgNWs	NA	0.5	140	643	NA	23	
PU/AgNWs	0.008	0.3	5.87	Yes	Failure	24	
PDMS/CNF	NA	0.8	0.04	Yes	Failure	25	
PU NF/AgNWs	NA	3.1	9,190	2,304 (25 °C)	~4	18	
PU/AgNWs	0.0012	1.2	3,668	Yes	~20	17	
NIPAM/AgNWs	NA	8	93	Yes	1.5	26	
PU/AgNWs	NA	0.5	~300	5,520 (35 °C)	Failure	15	
LM foam	NA	0.5 (compression)	390	Yes	NA	27	
SBS/LM	NA	18	100	724 (22 °C)	~1	19	
Challenges	<div>➤ Low stretchability</div> <div>➤ Strong electrical and mechanical coupling</div> <div>➤ Liquid metal-based composites suffer from smearing, leakage, and corrosion with metal components.</div>						
	Porous carbon-based composites						
	PEO/CNTs	~2 wt.%	1	0.018	NA	6	28
	PDMS/CNTs	NA	1.2	NA	No	>10	20
PU/CNTs	NA	0.8 (compression)	<0.01	Yes	Failure	29	
PU/CNTs	NA	3.2	NA	Yes	~14	30	
Challenges	<div>➤ Low electrical conductivity</div> <div>➤ Strong electrical and mechanical coupling</div> <div>➤ Limited strain-insensitive property</div>						
	Other porous composites						
	PU/MXene	NA	0.8 (compression)	<0.01	Yes	Failure	31
	Silk/PEDOT:PSS	NA	2.5	24	2,808 (37 °C)	4	16
Challenges	<div>➤ Low electrical conductivity</div> <div>➤ Large electrical hysteresis</div> <div>➤ Low stretchability</div>						
	PSPN	0.00062	7.5	8,152	4,424 (35 °C)	1.5	This work

Supplementary Table 2 Comparisons of the PSPN with existing nonporous conductive composites.

Materials	Percolation threshold (V_c)	Stretchability	Conductivity (S/cm)	Breathability	R/R ₀ @100%	Ref.
Metallic composites						
AgNWs/PU	0.018	2	7,330	No	>100	32
AgNWs/AgNPs/SEBS	NA	10	31,000	No	<2	10
Ag flakes/PEG/PANI/PTA	>0.05	10	60,000	No	<2	33
AgNWs/PS	0.00489	NA	10	No	NA	34
Ag flakes/fluorine rubber	0.046	4.1	4,000	No	NA	35
Au-AgNWs/SBS	0.0037	2.66	41,850	No	>10	36
AuNPs/PU (LBL*1)	0.162	0.16	6,800	No	>10	9
AuNPs/PU (VAF*1)	0.175	0.75	510			
AuNPs/PU (LBL*5)	0.162	1.15	11,000			
AuNPs/PU (VAF*5)	0.175	4.86	1,800			
Ni microparticles/self- healing polymer	0.15	NA	40	No	NA	37
Ag nanoflowers/PU	0.18	0.9	41,245	No	>100	11
		1.3	200			
AgNPs/PU	0.053	1.8	22,100	No	9	38
PS/Ag/PDMS	0.269	1.1	412	No	>300	39
Ag flakes/PU	0.062	2.1	200	No	~3	40
Ag flakes/PDMS	0.064	9	100			
Ag powder/PDMS	0.126	2.8	600	No	>10	41
LM/PU	0.38	>5	11,702	No	1.8	42
Challenges	➤ High percolation threshold					
	➤ Low stretchability					
	➤ High electrical and mechanical coupling					
	➤ Limited electrical durability (electrical degradation over repetitive strains)					
	➤ Nonbreathable (potentially cause skin inflammations and irritations)					
	➤ Liquid metal-based composites suffer from smearing, leakage, corrosion with metal components, and require large filler content					
Carbon-based composites						
Graphene/PU	0.05	0.25	0.005	No	Failure	43
CNTs/PU	0.005	13	10	No	NA	44
Graphene/polysilicone	0.0175	1	0.001	No	NA	45
Graphene nanoplates/Silicone	0.0149	2	0.5	No	>100	46

Challenges	➤	High percolation threshold				
	➤	Low electrical conductivity				
	➤	Nonbreathable (potentially cause skin inflammations and irritations)				
	➤	Limited strain-insensitive property				
Other composites						
PNAI/PAA-b-PBA	0.042	0.9	30	No	Failure	47
PANI/SEBS-g-MA	0.024	3	1,500	No	~10	48
Challenges	➤	Limited electrical conductivity				
	➤	Large electrical hysteresis				
	➤	Nonbreathable (potentially cause skin inflammations and irritations)				
	➤	Strong electrical-mechanical coupling				
PSPN (this work)	0.00062	7.5	8,152	Yes	1.5	
	➤	Ultralow percolation threshold (0.00062)				
	➤	Strain-insensitive electrical performance				
	➤	High electrical conductivity (highest average: 8,152 S/cm)				
	➤	Extreme stretchability (750%)				
	➤	Outstanding durability against abrasion and cyclic stretching tests				
	➤	Extraordinary breathability (WVTR: 4,424 g m ⁻² day ⁻¹)				
	➤	One-step in situ phase separation fabrication that eliminates ligand exchange process				

Captions for the Supplementary Videos:

Supplementary Video 1 Demonstration of PSPN mechanical resilience

Supplementary Video 2 ECG recording with strain-insensitive PSPN electrical wires

Supplementary Video 3 Wireless control of the implanted optoelectronic system

Supplementary Video 4 Wireless powering of the implanted optoelectronic system

Supplementary Reference

- 1 Hu, N., Karube, Y., Yan, C., Masuda, Z. & Fukunaga, H. Tunneling effect in a polymer/carbon nanotube nanocomposite strain sensor. *Acta Mater.* **56**, 2929-2936 (2008).
- 2 Simmons, J. G. Generalized formula for the electric tunnel effect between similar electrodes separated by a thin insulating film. *J. Appl. Phys.* **34**, 1793-1803 (1963).
- 3 Taya, M., Kim, W. & Ono, K. Piezoresistivity of a short fiber/elastomer matrix composite. *Mech. Mater.* **28**, 53-59 (1998).
- 4 Li, J. *et al.* Correlations between percolation threshold, dispersion state, and aspect ratio of carbon nanotubes. *Adv. Funct. Mater.* **17**, 3207-3215 (2007).
- 5 Li, J. & Zhang, S.-L. Finite-size scaling in stick percolation. *Phys. Rev. E* **80**, 040104 (2009).
- 6 Žeželj, M. & Stanković, I. From percolating to dense random stick networks: Conductivity model investigation. *Phys. Rev. B* **86**, 134202 (2012).
- 7 Stauffer, D. & Aharony, A. *Introduction to percolation theory*. (CRC press, 2018).
- 8 Taherian, R. Development of an equation to model electrical conductivity of polymer-based carbon nanocomposites. *ECS J. Solid State Sci. Technol.* **3**, M26 (2014).
- 9 Kim, Y. *et al.* Stretchable nanoparticle conductors with self-organized conductive pathways. *Nature* **500**, 59-63 (2013).
- 10 Jung, D. *et al.* Adaptive self-organization of nanomaterials enables strain-insensitive resistance of stretchable metallic nanocomposites. *Adv. Mater.* **34**, 2200980 (2022).
- 11 Ma, R., Kang, B., Cho, S., Choi, M. & Baik, S. Extraordinarily high conductivity of stretchable fibers of polyurethane and silver nanoflowers. *ACS Nano* **9**, 10876-10886 (2015).
- 12 Tang, L., Shang, J. & Jiang, X. Multilayered electronic transfer tattoo that can enable the crease amplification effect. *Sci. Adv.* **7**, eabe3778 (2021).
- 13 Ohm, Y. *et al.* An electrically conductive silver–polyacrylamide–alginate hydrogel composite for soft electronics. *Nat. Electron.* **4**, 185–192 (2021).
- 14 Son, D. *et al.* An integrated self-healable electronic skin system fabricated via dynamic reconstruction of a nanostructured conducting network. *Nat. Nanotechnol.* **13**, 1057-1065 (2018).
- 15 Zhou, W. *et al.* Gas-permeable, ultrathin, stretchable epidermal electronics with porous electrodes. *ACS Nano* **14**, 5798–5805 (2020).
- 16 Li, Q. *et al.* Highly thermal-wet comfortable and conformal silk-based electrodes for on-skin sensors with sweat tolerance. *ACS Nano* **15**, 9955–9966 (2021).
- 17 Zhu, H.-W. *et al.* Printable elastic silver nanowire-based conductor for washable electronic textiles. *Nano Res.* **13**, 2879-2884 (2020).
- 18 Jiang, Z. *et al.* Highly stretchable metallic nanowire networks reinforced by the underlying randomly distributed elastic polymer nanofibers via interfacial adhesion improvement. *Adv. Mater.* **31**, 1903446 (2019).
- 19 Ma, Z. *et al.* Permeable superelastic liquid-metal fibre mat enables biocompatible and monolithic stretchable electronics. *Nat. Mater.* **20**, 859–868 (2021).
- 20 Oh, J. *et al.* Pressure insensitive strain sensor with facile solution-based process for tactile sensing applications. *ACS Nano* **12**, 7546-7553 (2018).
- 21 Kang, H., Kim, Y., Cheon, S., Yi, G.-R. & Cho, J. H. Halide welding for silver nanowire network

- electrode. *ACS Appl. Mater. Interfaces* **9**, 30779-30785 (2017).
- 22 Oh, J. Y., Lee, D. & Hong, S. H. Ice-templated bimodal-porous silver nanowire/PDMS
nanocomposites for stretchable conductor. *ACS Appl. Mater. Interfaces* **10**, 21666-21671 (2018).
- 23 Yao, S. *et al.* Ultrasoft porous 3D conductive dry electrodes for electrophysiological sensing and
myoelectric control. *Adv. Mater. Technol.* **7**, 2101637 (2022).
- 24 Zeng, Z. *et al.* Ultralight and flexible polyurethane/silver nanowire nanocomposites with
unidirectional pores for highly effective electromagnetic shielding. *ACS Appl. Mater. Interfaces* **9**,
32211-32219 (2017).
- 25 Wu, S. *et al.* Novel electrically conductive porous PDMS/carbon nanofiber composites for
deformable strain sensors and conductors. *ACS Appl. Mater. Interfaces* **9**, 14207-14215 (2017).
- 26 Song, P., Qin, H., Gao, H. L., Cong, H. P. & Yu, S. H. Self-healing and superstretchable conductors
from hierarchical nanowire assemblies. *Nat. Commun.* **9**, 2786 (2018).
- 27 Peng, Y., Liu, H., Li, T. & Zhang, J. Hybrid metallic foam with superior elasticity, high electrical
conductivity, and pressure sensitivity. *ACS Appl. Mater. Interfaces* **12**, 6489-6495 (2020).
- 28 Bian, Y. & Li, Y. Porous conductive elastomeric composites with carbon nanotubes suspended in
the narrow pores from co-continuous polymer blend nanocomposites. *Compos. Sci. Technol.* **218**,
109116 (2022).
- 29 Wang, X. *et al.* Flexible and high-performance piezoresistive strain sensors based on multi-walled
carbon nanotubes@ polyurethane foam. *RSC Adv.* **12**, 14190-14196 (2022).
- 30 Wang, X. *et al.* A highly stretchable carbon nanotubes/thermoplastic polyurethane fiber-shaped
strain sensor with porous structure for human motion monitoring. *Compos. Sci. Technol.* **168**, 126-
132 (2018).
- 31 Chen, Q., Gao, Q., Wang, X., Schubert, D. W. & Liu, X. Flexible, conductive, and anisotropic
thermoplastic polyurethane/polydopamine/MXene foam for piezoresistive sensors and motion
monitoring. *Compos. Part A Appl. Sci. Manuf.* **155**, 106838 (2022).
- 32 Lu, Y. *et al.* High-performance stretchable conductive composite fibers from surface-modified
silver nanowires and thermoplastic polyurethane by wet spinning. *ACS Appl. Mater. Interfaces* **10**,
2093-2104 (2018).
- 33 Wang, T., Liu, Q., Liu, H., Xu, B. & Xu, H. Printable and highly stretchable viscoelastic conductors
with kinematically reconstructed conductive pathways. *Adv. Mater.* **34**, 2202418 (2022).
- 34 Sureshkumar, M., Na, H. Y., Ahn, K. H. & Lee, S. J. Conductive nanocomposites based on
polystyrene microspheres and silver nanowires by latex blending. *ACS Appl. Mater. Interfaces* **7**,
756-764 (2015).
- 35 Matsuhisa, N. *et al.* Printable elastic conductors by in situ formation of silver nanoparticles from
silver flakes. *Nat. Mater.* **16**, 834-840 (2017).
- 36 Choi, S. *et al.* Highly conductive, stretchable and biocompatible Ag-Au core-sheath nanowire
composite for wearable and implantable bioelectronics. *Nat. Nanotechnol.* **13**, 1048-1056 (2018).
- 37 Tee, B. C., Wang, C., Allen, R. & Bao, Z. An electrically and mechanically self-healing composite
with pressure-and flexion-sensitive properties for electronic skin applications. *Nat. Nanotechnol.*
7, 825-832 (2012).
- 38 Kang, Y. *et al.* High-resolution printable and elastomeric conductors from strain-adaptive

- assemblies of metallic nanoparticles with low aspect ratios. *Small* **16**, 2004793 (2020).
- 39 Hu, Y. *et al.* A low-cost, printable, and stretchable strain sensor based on highly conductive elastic
composites with tunable sensitivity for human motion monitoring. *Nano Res.* **11**, 1938-1955 (2018).
- 40 Sun, H., Han, Z. & Willenbacher, N. Ultrastretchable conductive elastomers with a low percolation
threshold for printed soft electronics. *ACS Appl. Mater. Interfaces* **11**, 38092-38102 (2019).
- 41 Larmagnac, A., Eggenberger, S., Janossy, H. & Vörös, J. Stretchable electronics based on Ag-
PDMS composites. *Sci. Rep.* **4**, 7254 (2014).
- 42 Liu, Y., Ji, X. & Liang, J. Rupture stress of liquid metal nanoparticles and their applications in
stretchable conductors and dielectrics. *npj Flex. Electron.* **5**, 11 (2021).
- 43 Liu, H. *et al.* Electrically conductive thermoplastic elastomer nanocomposites at ultralow graphene
loading levels for strain sensor applications. *J. Mater. Chem. C* **4**, 157-166 (2016).
- 44 Koerner, H. *et al.* Deformation–morphology correlations in electrically conductive carbon
nanotube—thermoplastic polyurethane nanocomposites. *Polymer* **46**, 4405-4420 (2005).
- 45 Boland, C. S. *et al.* Sensitive electromechanical sensors using viscoelastic graphene-polymer
nanocomposites. *Science* **354**, 1257-1260 (2016).
- 46 Wang, Y., Zhu, L., Mei, D. & Zhu, W. A highly flexible tactile sensor with an interlocked truncated
sawtooth structure based on stretchable graphene/silver/silicone rubber composites. *J. Mater. Chem.*
C **7**, 8669-8679 (2019).
- 47 Ding, H. *et al.* Elastomeric conducting polyaniline formed through topological control of molecular
templates. *ACS Nano* **10**, 5991-5998 (2016).
- 48 Stoyanov, H., Kolloosche, M., Risse, S., Waché, R. & Kofod, G. Soft conductive elastomer materials
for stretchable electronics and voltage controlled artificial muscles. *Adv. Mater.* **25**, 578-583 (2013).